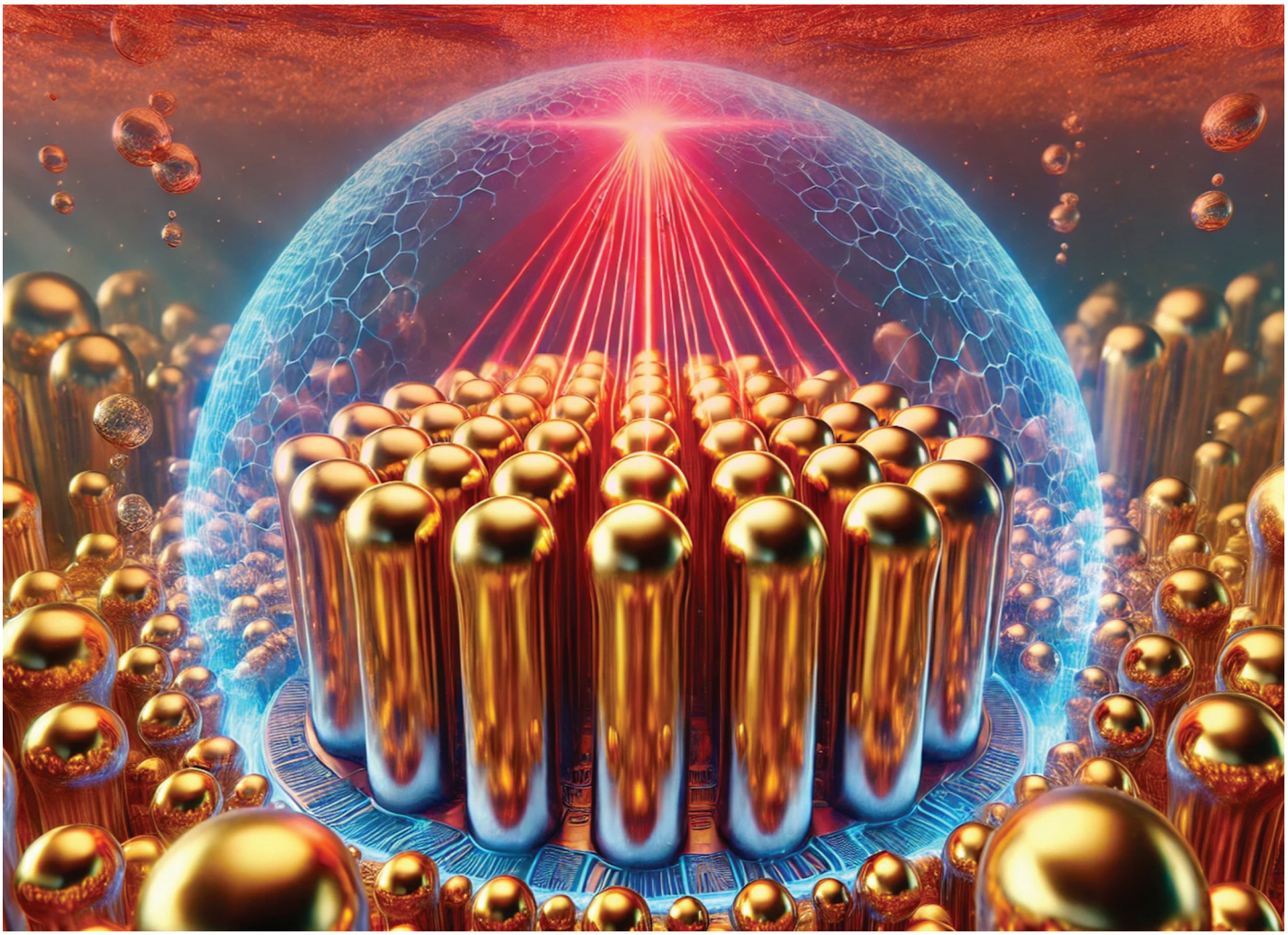

Showcasing research from the groups of Prof. Ivan Jabin at the Laboratoire de Chimie Organique and Prof. Gilles Bruylants at the Engineering of Molecular Nanosystems Laboratory, Université libre de Bruxelles, Brussels, Belgium.

Calixarene-coated gold nanorods as robust photothermal agents

Gold nanorods were functionalized with an innovative calix[4]arene-based coating that significantly bolsters their stability under sustained laser exposure, while facilitating effective conjugation. These fortified and conjugable gold nanorods are promising candidates for applications in the context of photothermal therapy, where structural integrity and durability are essential. Cover design by V. Lepeintre; created using Adobe Firefly. The authors thank the Fondation Universitaire for its financial support for the cover art.

As featured in:

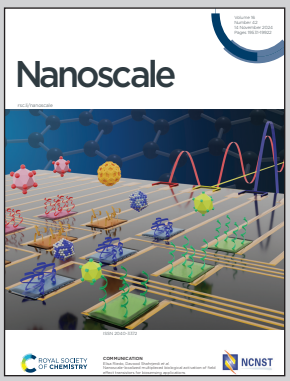

See Gilles Bruylants, Ivan Jabin *et al.*, *Nanoscale*, 2024, **16**, 19692.

ROYAL SOCIETY OF CHEMISTRY

rsc.li/nanoscale

Registered charity number: 207890

Nanoscale

PAPER

Check for updates

Cite this: *Nanoscale*, 2024, **16**, 19692

Calixarene-coated gold nanorods as robust photothermal agents†

Victor Lepeintre, [a,b] Franck Camerel,[c] Corinne Lagrost,[c,d] Maurice Retout, [a] Gilles Bruylants *[a] and Ivan Jabin *[b]

Received 1st June 2024,
Accepted 27th August 2024

DOI: 10.1039/d4nr02296c

rsc.li/nanoscale

Gold nanorods (AuNRs) hold considerable promise for their use in biomedical applications, notably in the context of photothermal therapy (PTT). Yet, their anisotropic nature presents a notable hurdle. Under laser irradiation, these structures are prone to deformation, leading to changes in their optical and photothermal properties over time. To overcome this challenge, an efficient strategy involving the use of calix[4]arene-tetradiazonium salts for stabilizing AuNRs has been implemented. These molecular platforms are capable of irreversible grafting onto surfaces through the reduction of their diazonium groups, thereby resulting in the formation of exceedingly robust organic monolayers. This innovative coating strategy not only ensures enduring stability but also facilitates conjugation of AuNRs. This study showcases the superiority of these fortified AuNRs over conventional counterparts, notably exhibiting exceptional resilience even under sustained laser exposure in the context of PTT. By bolstering the stability and reliability of AuNRs in PTT, our approach holds the potential to drive significant advancements in the field.

Introduction

Gold nanorods (AuNRs) have emerged as highly promising materials for various biomedical *in vivo* applications, including as photothermal agents (PTAs), bioimaging contrast agents and drug delivery systems.[1–4] Beyond the compelling attributes inherent to gold nanoparticles (AuNPs), such as their excellent biocompatibility and diverse surface chemistries, the optical properties of AuNRs are amenable to precise modulation.[3,5] The optical behaviour of gold nanostructures is underpinned by the Localized Surface Plasmon Resonance (LSPR) phenomenon, arising from the collective oscillations of their conduction electrons in response to incident electromagnetic fields.[3,5] AuNRs exhibit dual LSPR modes, namely transverse and longitudinal, the latter of which can be adeptly tailored by manipulating the aspect ratio (AR) of the rods.[1–3,5]

For high AR (above 3), the longitudinal LSPR band lies in the near-infrared (NIR) spectral region, which engenders a plethora of opportunities for *in vivo* applications, including photothermal therapy and non-invasive optical imaging.[1,2] This spectral window between 650 and 1350 nm is often acknowledged as the "therapeutic window" or "optical transparency window", given its minimal light absorbance by water, hemoglobin, and other endogenous molecules, hence enabling enhanced light penetration into tissues compared to visible light.[1,2] Photothermal therapy (PTT) is a promising non-invasive cancer treatment strategy leveraging the conversion of light to heat by PTAs for thermal ablation of cancer cells.[4,6,7] AuNRs possess several qualities that make them excellent PTAs including intense optical extinction coefficient in the NIR region, high photothermal conversion efficiency, long circulation time, ease in functionalization, and high biocompatibility, provided that their coating does not induce toxicity.[4,6,7] However, one limitation is their anisotropic structure that is susceptible to deformation under laser irradiation leading to the alteration of their optical and photothermal properties.[8,9]

AuNRs synthesized through the prevalent seed-mediated growth approach, which occurs in the presence of cetyltrimethylammonium bromide (CTAB), exhibit limited direct utility in biomedical applications, due to their the inherent cytotoxicity associated with CTAB.[10–12] The optimal solution involves an efficient ligand exchange strategy to remove the CTAB molecules that imparts chemical functionality compatible with conjugation chemistry, ensures colloidal stability both

[a]*Engineering of Molecular NanoSystems, Ecole Polytechnique de Bruxelles, Université Libre de Bruxelles (ULB), Avenue F. D. Roosevelt 50, CP165/64, B-1050 Brussels, Belgium. E-mail: Gilles.Bruylants@ulb.be*
[b]*Laboratoire de Chimie Organique, Université Libre de Bruxelles (ULB), Avenue F. D. Roosevelt 50, CP160/06, B-1050 Brussels, Belgium. E-mail: Ivan.Jabin@ulb.be*
[c]*Univ. Rennes, CNRS, ISCR – UMR 6226, F-35000 Rennes, France*
[d]*Univ. Rennes, CNRS, ScanMAT – UAR 2025, F-35000 Rennes, France*

†Electronic supplementary information (ESI) available: Additional methods, reaction condition optimizations, TEM images, SAED pattern, EDX spectrum, SERS spectra, UV-vis spectra, temperature profiles, DLS plots, XPS spectra and photographs of experimental setup. See DOI: https://doi.org/10.1039/d4nr02296c

This journal is © The Royal Society of Chemistry 2024

during and after functionalization, and retain water dispersibility of functionalized AuNRs.[13] Commonly employed strategies include the use of biocompatible ligands through either electrostatic interaction or thiol-based functionalization.[10,14,15] Typically, thiolated PEG molecules are efficiently used to substitute CTAB, where thiol groups chemisorb onto the AuNRs' surface through Au–S bonds.[15] The introduction of PEG chains onto AuNRs notably enhances their stability and biocompatibility.[15] However, the use of large thiolated PEG chains can result in a thick coating, causing a greater separation between the gold surface, the conjugated bioactive molecules and the surrounding medium, which, depending on the targeted application, can be problematic (*e.g.* photodynamic therapy, surface-enhanced spectroscopy-based sensing or plasmonic coupling-based applications).[13] Additionally, the Au–S bonds are susceptible to thermolysis, can be subjected to irreversible oxidation in biological systems, and can be exchanged with endogenous thiol containing (bio)molecules such as glutathione, impacting the stability of the AuNRs.[16–18] Conversely, electrostatic physisorption of (poly)electrolytes, such as citrate, polystyrene sulfonate (PSS), or polyethylenimine (PEI), emerges as an alternative, offering colloidal stability and a platform for immobilizing biomolecules through electrostatic interactions.[10,14,19,20] Nevertheless, the binding energies between (poly)electrolytes and the surface of AuNRs often exhibit variability under physiological conditions, leading to partial leaching of the physisorbed ligands and the formation of aggregates, especially under irradiation.[13,14] Another strategy involves AuNR encapsulation with inorganic or carbon-based materials such as mesoporous silica, polydopamine or proteins (*e.g.* albumin).[10,19,21] However, these strategies often prove challenging regarding post-functionalization with bioactive molecules, and generally result in the formation of a thick layer around the AuNRs which, as mentioned earlier, could be detrimental in some applications.[10,19] In addition, these approaches only cover the CTAB layer rather than replacing it, thereby raising concerns about toxicity due to the persistent presence of CTAB within the assembly.[10,19]

To address these challenges, we have envisioned an alternative approach for the functionalization of AuNRs, involving the use of calix[4]arene-tetradiazonium salts.[22–24] Calixarenes are conical macrocyclic platforms capable of being functionalized on both their large and small rims.[25] Those used in this work are equipped on the large rim with four diazonium groups that can be reduced to the corresponding aryl radicals, enabling their attachment to various types of metallic nanoparticles *via* multiple, strong and irreversible Au–C covalent bonds.[26–28] The energy of the Au–C bond has been calculated to be 14.2 kJ mol^{-1} (3.4 kcal mol^{-1}) higher than that of the Au–S bond, resulting in a more robust organic layer on the surface compared to coatings formed using thiols.[29,30] It has previously been reported that AuNRs can be functionalized with simple aryl diazonium salts, however this strategy generally results in uncontrolled polymerization caused by the reaction of aryl radicals with the already-grafted aryl molecules.[31,32] This leads to the formation of thick and loosely-packed multilayers constituted of arborescent poly(phenylene) structures with a reduced number of anchoring points to the surface.[31–33] In contrast, the use of calix[4]arene-tetradiazonium salts offers the opportunity to form thin and dense monolayers, owing to the *meta* positions of the aryl groups being substituted with methylene bridges, thus avoiding any further polymerization.[22–24] Furthermore, because the calixarenes are equipped with four diazonium groups, each macrocycle can form up to four Au–C bonds with the surface, resulting in an increased density of anchoring points and much more robust coating compared to the use of simple aryl diazonium salts.[22–24] This calix[4]arene-based functionalization strategy has been successfully employed and reported for various silver nanostructures, such as nanoparticles, nanoplates and gold–silver core–shell nanoparticles, which are notoriously hard to stabilize due to silver's susceptibility to oxidation.[27,28,34] The small rim of the calixarene used in this work bears four appending carboxyl groups ($X_4C_4(N_2^+)_4$) (Scheme 1).[22,26] These groups ensure the electrostatic stabilization and aqueous dispersibility of the nanoparticles, and can subsequently facilitate the coupling of various amine-terminated (bio)molecules, enabling opportunities for specific targeting, drug delivery, and sensing applications.[26–28]

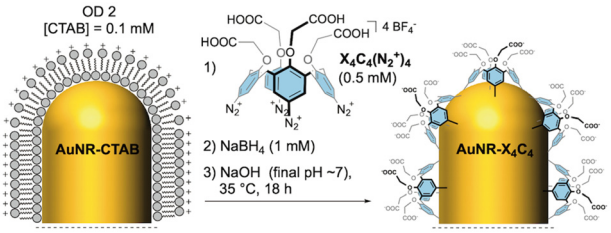

Scheme 1 Synthesis of AuNR-X_4C_4 from AuNR-CTAB through a ligand exchange procedure.

In this work, we have developed a new generation of calixarene-coated AuNRs (AuNR-X_4C_4) using the calix[4]arene-based functionalization strategy. The (photo)chemical and colloidal stabilities of these calixarene-coated AuNRs were compared to those of AuNRs functionalized with monodentate thiolated polyethylene glycol (PEG) molecules (AuNR-S-PEG_8-COOH) or stabilized with citrate molecules (AuNR-citrate), commonly used for biomedical applications. Covalent post-functionalization of the calixarene-coated AuNRs was studied by coupling an amine-terminated fluorophore through carbodiimide cross-linking chemistry. Finally, we examined the photothermal properties and stability of AuNR-X_4C_4 and evaluated the improvement compared to AuNRs with different coatings.

Experimental section

Functionalization of AuNRs with $X_4C_4(N_2^+)_4$

$X_4C_4(N_2^+)_4$ was dissolved in ultrapure water to prepare a 5 mM stock solution. To 10 mL of AuNR-CTAB (OD_{LSPR} = 2, stabilized in 0.1 mM CTAB) under vigorous stirring at 35 °C, 1 mL

$X_4C_4(N_2^+)_4$ (5 mM in water) was added dropwise followed by 100 μL freshly prepared ice-cold $NaBH_4$ (100 mM in water), the pH of the solution at this stage should be around 2.5. After 5 minutes of stirring, the pH of the solution was adjusted to 7.0 by stepwise additions of 50 μL NaOH (100 mM in water) spaced by at least 2 min initially, then 10 μL additions when approaching the desired pH value (above 6). A total added volume of approximately 230 μL NaOH (100 mM in water) was added to reach pH 7.0. The pH must be measured after each addition to ensure that it does not exceed 7.5, as exceeding this value may cause destabilization of the AuNR suspension. The mixture was then stirred overnight (18 h) at 35 °C before addition of 50 μL NaOH (1 M in water). The functionalized AuNRs (AuNR-X_4C_4) were centrifuged four times at 12 000*g* for 20 min and resuspended with 10 mL NaOH (5 mM in water) thrice and finally with 10 mL ultrapure water. Different AuNR batches were synthesized for characterization (initial AR = 4.1 ± 0.4), chemical and colloidal stability (initial AR = 3.6 ± 0.7) and photothermal studies (initial AR = 4.3 ± 0.4).

Preparation of AuNR-citrate

The citrate-coated AuNRs were prepared with a revised polystyrene sulfonate (PSS) replacement method described by Mehtala *et al.*[14] To 10 mL of AuNR-CTAB (OD_{LSPR} = 3, stabilized in 0.1 mM CTAB), 1.765 mL of a PSS (1 wt% in water, M_W ≈ 70 kDa) and NaCl (5 mM in water) mixture was added. The solution was left undisturbed at room temperature for at least 1 h. The AuNRs were centrifuged at 6000*g* for 30 min, the supernatant was discarded and the pellet was redispersed with 10 mL ultrapure water followed by the addition of 1.765 mL PSS (1 wt% in water) and NaCl (5 mM in water). The PSS incubation and centrifugation were repeated twice more to yield PSS-stabilized AuNRs. The AuNR suspension was then centrifuged at 6000*g* for 30 min, the supernatant was discarded and the pellet was redispersed with 10 mL trisodium citrate (5 mM in water). The solution was left undisturbed at room temperature for at least 12 h. The AuNRs were then centrifuged at 5500*g* for 20 min in 1.5 mL centrifuge tubes, the supernatants were discarded and replaced with a total of 2.5 mL trisodium citrate (5 mM in water) to yield AuNR-citrate.

Functionalization of AuNRs with HS-PEG_8-COOH

AuNR-citrate were functionalized with heterobifunctional polyethylene glycol ended by thiol and carboxylic acid groups (HS-PEG_8-COOH) *via* a ligand exchange method. To 10 mL of AuNR-citrate (OD_{LSPR} = 5, stabilized in 5 mM trisodium citrate), 1 mL HS-PEG_8-COOH (5 mM in water) was added under stirring. After 16 hours of stirring at room temperature, the functionalized AuNRs (AuNR-S-PEG_8-COOH) were centrifuged four times at 12 000*g* for 20 min and resuspended with 10 mL SDS (1 wt% in water) twice, then with 10 mL NaOH (5 mM in water) and finally with 10 mL ultrapure water.

Conjugation of the AuNR-X_4C_4 with Cyanine5.5 amine

In a 1.5 mL Eppendorf tube, 500 μL AuNR-X_4C_4 (OD_{LSPR} = 1) were suspended in MES buffer (10 mM in water; pH 5.8). To this, 50 μL EDC (6 mM in water) and 50 μL sulfo-NHS (10 mM in water) were added and the mixture was stirred in a thermomixer at 1000 rpm for 15 min. Then, 166.7 μL of DMSO was added to ensure the fluorophore solubility (25 v/v% DMSO) before an appropriate volume of Cyanine5.5 amine (330 μM in DMSO) was added to reach 10 000 equivalents per AuNR. The temperature was then increased to 50 °C, and the mixture was stirred at 1000 rpm for 4 h. At the end of the reaction, 7.5 μL NaOH (1 M in water) and 150 μL SDS (10 wt% in water) were added and the volume was completed to 1.5 mL with ultrapure water. AuNRs were then centrifuged four times at 12 000*g* for 20 min and resuspended with 1.5 mL SDS (1 wt% in water) thrice and finally with 500 μL ultrapure water.

Photothermal conversion experiments

The photothermal studies were done using an 808 nm laser (Changchun New Industries Optoelectronics, FC-W-808A-10W) in a 3500 μL special optical glass cuvette (Hellma, 100-OS, Schott N-K5 glass). The temperature was measured with a thermocouple (PerfectPrime, TC0520) with an accuracy of ±0.1 °C and data were recorded and saved on a computer with the dedicated software SE520. The thermocouple measured the solution temperature and was immersed in such a position that direct irradiation by the laser was avoided. The power intensity of the laser could be adjusted externally (0–10 W). The output power was independently calibrated using an optical power meter. In a typical experiment, AuNRs (2 mL, OD_{808} = 0.5) were irradiated at 3 W cm^{-2} for 18 min before turning the laser off for 18 min, and the temperature was measured every second throughout the entire run without stirring. The glass cuvette was placed in a 3D-printed white PLA cuvette holder with a 1 cm diameter aperture for laser irradiation and aeration grids on the sides. Photographs of the setup are shown in Fig. S16.† For multiple cycles experiments, five consecutive 24-minute cycles were performed (12 min heating and 12 min cooling). Photothermal conversion efficiencies were calculated using the method reported by Roper *et al.* (see the Supplementary Methods section of the ESI† for an example of the detailed calculation).[35]

Results and discussion

Synthesis of gold nanorods

CTAB-stabilized AuNRs (AuNR-CTAB) were synthesized with an optimized silver-assisted seed-mediated growth method, wherein the symmetry-breaking event is decoupled from the seeded growth process.[36] This approach results in narrower size distributions of the final AuNRs and improved shape yield compared to standard syntheses.[36] Initially, spherical gold seeds of a few nanometres were formed through accelerated reduction of chloroauric acid ($HAuCl_4$) by sodium borohydride ($NaBH_4$) in a micellar solution of CTAB and 1-decanol. These spherical gold seeds underwent further growth into small anisotropic seeds (*i.e.* symmetry-breaking event). Subsequently, these anisotropic seeds were used for the synthesis of

 This journal is © The Royal Society of Chemistry 2024

AuNR-CTAB (Fig. S1A†). Using this method, AuNR-CTAB with narrow LSPR bands and a maximum absorption wavelength of 843 nm were successfully synthesized (Fig. S1B†). Transmission electron microscopy (TEM) images revealed dimensions of 60.4 ± 5.0 × 13.8 ± 1.1 nm (AR = 4.4 ± 0.4) (Fig. S1C†).

Synthesis and characterization of calix[4]arene-coated AuNRs (AuNR-X_4C_4)

The reductive grafting of $X_4C_4(N_2^+)_4$ was performed by ligand exchange on AuNR-CTAB. The functionalization protocol is based on previously documented methods applied to various metallic nanomaterials.[26,28,37,38] Briefly, an aqueous solution of $X_4C_4(N_2^+)_4$ was added to AuNR-CTAB, followed by an aqueous solution of $NaBH_4$ in controlled pH conditions (Scheme 1). $NaBH_4$ is known to reduce the calix[4]arene-tetradiazonium molecules to the corresponding aryl radicals, which are the reactive species capable of grafting onto AuNRs, but it also probably facilitates the removal of CTAB from the surface of AuNRs. It has indeed previously been described that the hydride ions derived from sodium borohydride have a high affinity for gold and rapidly replace CTAB on the surface of AuNRs.[39] The surface-bound hydride ions eventually react with water to form H_2 gas which leads to their removal from the AuNR surface, leaving a capping agent-free surface, which facilitates the grafting of calixarene molecules. It is noteworthy that critical parameters were identified to ensure efficient and reproducible ligand exchange, as well as to maintain colloidal stability during the functionalization (Table S1†). The free CTAB concentration was optimized at 0.1 mM to facilitate efficient ligand exchange without inducing AuNR aggregation. Similarly, an optimal AuNR concentration of ~0.5 nM (OD_{LSPR} = 2) was chosen to prevent aggregation. A pH reaction range of 6.9–7.1 was identified as ideal, avoiding both the instability of starting AuNR-CTAB in basic conditions and the gradual aggregation of AuNRs due to the protonation of carboxyl groups that disrupts the electrostatic stabilization during ligand exchange. The optimized ligand exchange procedure was repeated ten times yielding the same results, proving the reproducibility of the synthesis.

The AuNR-X_4C_4 were characterized using various analytical techniques, including TEM, ζ-potential analysis, UV-visible absorption, attenuated total reflection Fourier-transform infrared (ATR-FTIR) and surface-enhanced Raman (SERS) spectroscopies (Fig. 1). UV-visible absorption spectra of AuNRs before and after calixarene functionalization exhibited sharp LSPR bands, indicating the presence of well-dispersed AuNRs that maintained their colloidal state during ligand exchange

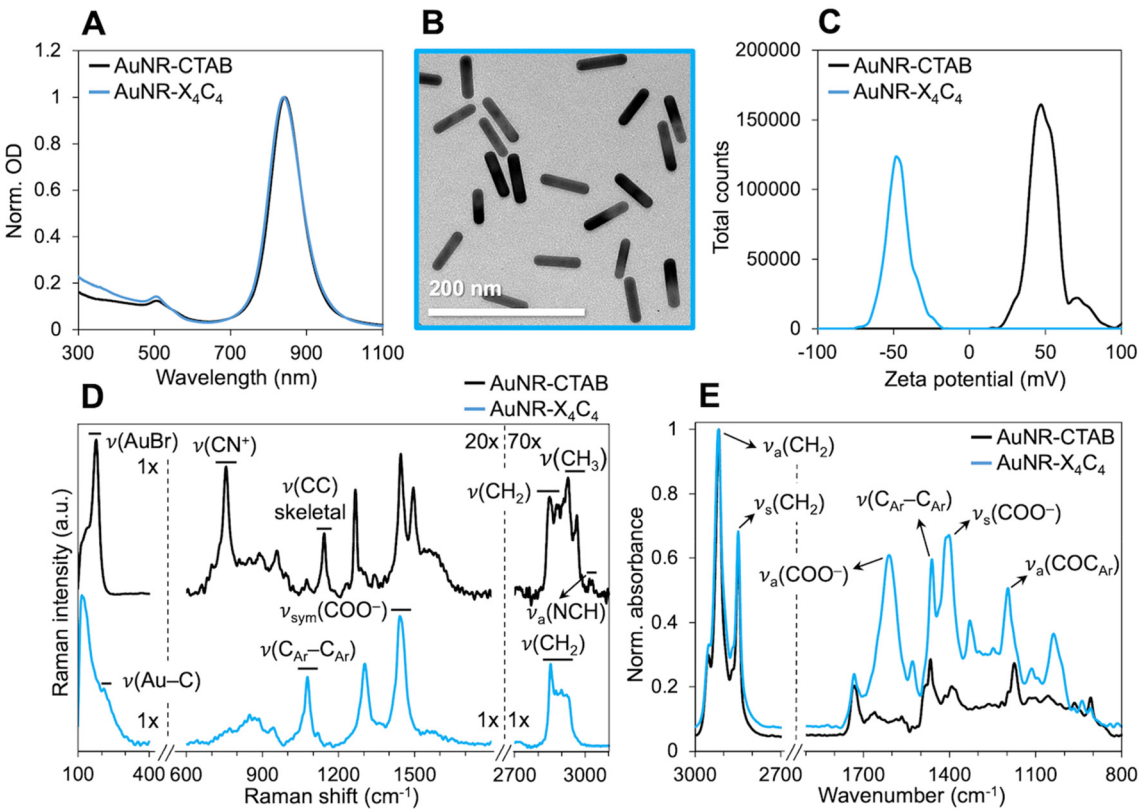

Fig. 1 Characterization of AuNR-CTAB and AuNR-X_4C_4. (A) UV-visible absorption spectra of AuNR-CTAB (black) and AuNR-X_4C_4 (blue). (B) TEM image of AuNR-X_4C_4. (C) ζ-Potential distributions of AuNR-CTAB (black) and AuNR-X_4C_4 (blue) measured at pH 7. (D) SERS spectra of AuNR-CTAB (black) and AuNR-X_4C_4 (blue) with tentative Raman band assignments, the spectra are scaled for clarity and the respective magnifications are displayed for each region. (E) Normalized ATR-FTIR absorption spectra of AuNR-CTAB (black) and AuNR-X_4C_4 (blue) with IR band assignments.

(Fig. 1A). The maximum absorption wavelength of the AuNR-CTAB slightly shifted from 843 nm to 840 nm upon functionalization. This slight hypsochromic shift could be attributed to several factors such as the slight decrease of the average AR observed upon functionalization (Fig. S2 and S3†), the presence of $NaBH_4$ during the ligand exchange, which is known to cause hypsochromic shifts for AuNRs,[39] or a possible modification of the dielectric environment at the surface of AuNRs. The increase of optical density in the near-UV region is likely due to the light absorption of the calixarenes grafted onto AuNRs, as suggested by the UV-visible absorption spectrum of the $X_4C_4(N_2^+)_4$ aqueous solution, that unlike CTAB, displays intense absorption in that region (Fig. S4†). TEM analysis corroborated these findings, revealing similar average width, length, and shape of AuNRs before functionalization (60.4 ± 5.0 × 13.8 ± 1.1 nm, AR = 4.4 ± 0.4) and after functionalization (61.4 ± 4.7 × 14.9 ± 1.1 nm, AR = 4.1 ± 0.4) (Fig. 1B and S1C, S2, S3†). High-resolution TEM (HRTEM) images of AuNR-X_4C_4 revealed fringe spacing of 2.39 and 2.08 Å, characteristic of the (1,1,1) and (2,0,0) lattice planes of gold, respectively (Fig. S5A and B†). The selected area electron diffraction (SAED) pattern of AuNR-X_4C_4 confirmed the presence of face-centred cubic (FCC) gold ($Fm\bar{3}m$ space group) (Fig. S5C†). Moreover, the energy-dispersive X-ray (EDX) spectrum of AuNR-X_4C_4 revealed, as expected, the presence of gold and carbon in high abundance, while no bromine was detected, suggesting the efficient removal of CTAB from the surface of the AuNRs (Fig. S5D†). ζ-Potential measurements confirmed the ligand exchange, with a shift from positive values (50.0 ± 2.6 mV) to negative values (−43.6 ± 2.8 mV) upon AuNR functionalization (Fig. 1C). This shift aligns with the replacement of positively charged CTAB with negatively charged calixarenes, a noteworthy observation given the challenges associated with achieving one-step ζ-potential inversion, often resulting in aggregation and low recovery yields.[14] Similarly, SERS analysis revealed new Raman bands upon AuNR functionalization, suggesting the presence of calixarenes on the AuNR surface (Fig. 1D). Tentative Raman band assignments were performed for AuNR-X_4C_4, with Au–C stretching at 210 cm^{-1},[40] aromatic ring stretching at 1077 cm^{-1}, carboxylate symmetric stretching at 1441 cm^{-1}, and CH_2 symmetric and asymmetric stretching at 2853 cm^{-1} and 2876 cm^{-1}, respectively. The Raman band at 117 cm^{-1}, which was also visible for AuNR-CTAB as a shoulder peak, is attributed to gold lattice vibrations.[41] For AuNR-CTAB, characteristic cetyltrimethylammonium (CTA^+) Raman bands were visible such as CN^+ stretching at 756 cm^{-1}, skeletal CC stretching at 1142 cm^{-1}, methyl/methylene CH_x stretching modes at 2800 to 3000 cm^{-1}, and NCH asymmetric stretching at 3018 cm^{-1}.[21] Notably, the very intense Raman band at 180 cm^{-1}, attributed to the surface-bound bromide counterion ($AuBr^-$), is clearly visible, indicating a surface-bound interlayer of bromides between the CTA^+ bilayer and the gold surface.[21,42] After calixarene functionalization, this signal vanishes indicating efficient CTAB removal. Similarly, characteristic signals of CTA^+, such as CN^+ stretching and skeletal CC stretching, also vanished upon functionalization, further confirming CTAB removal. Original full range and unscaled SERS spectra can be found in the ESI (Fig. S6†). ATR-FTIR spectroscopy validated the presence of calixarenes at the surface of the AuNRs, with characteristic IR absorption bands visible at 1461 cm^{-1} for aromatic ring stretching, 1197 cm^{-1} for asymmetric COC_{Ar} stretching, 1611 and 1403 cm^{-1} for asymmetric and symmetric carboxylate stretching respectively (Fig. 1E).[38]

Chemical and colloidal stability of AuNR-X_4C_4

The chemical and colloidal stabilities of AuNRs stabilized by calixarenes, thiolated PEG molecules (*i.e.* HS-PEG_8-COOH), citrate or CTAB were assessed using UV-visible absorption spectroscopy (see the Experimental section for the synthesis procedures of AuNR-citrate and AuNR-S-PEG_8-COOH). The corresponding absorption spectra of the colloidal AuNR suspensions were compared before and after exposure to different physicochemical stresses.

Under acidic conditions (pH 3), all three types of carboxyl-terminated AuNRs experienced aggregation due to the protonation of carboxylate groups, leading to a depletion of the electrostatic repulsion (Fig. 2A). Notably, a bathochromic shift occurred over time in acidic conditions for AuNR-X_4C_4 and AuNR-citrate, possibly attributable to end-to-end aggregation. In contrast, a hypsochromic shift was observed for AuNR-S-PEG_8-COOH, possibly suggesting side-to-side aggregation. In contrast to AuNR-citrate, the aggregation observed for AuNR-X_4C_4 was completely reversible upon shifting to basic conditions (pH 11), even after several successive pH variation cycles. For AuNR-S-PEG_8-COOH, while the aggregation was partially reversible, the maximum optical density of the longitudinal LSPR band (OD_{LSPR}) decreased, and absorbance at higher wavelength increased with successive cycles, indicating the formation of irreversible aggregates. AuNR-CTAB were stable under acidic conditions but irreversibly aggregated upon shifting to basic conditions (Fig. S7A†).

The coating density and robustness were then evaluated with a fluoride-induced aggregation test (Fig. 2B).[43] The different AuNRs colloids were incubated with 200 mM KF, and their UV-visible absorption spectra were recorded at different time intervals throughout 1 h. For AuNR-X_4C_4, the UV-visible absorption spectra remained mostly unchanged, with only a slight decrease of the OD_{LSPR} over time, characteristic of a dense and robust coating. Similarly, AuNR-CTAB also experienced little aggregation, showcasing the density of the CTAB bilayer coating and its high affinity for the gold surface (Fig. S7B†). However, progressive aggregation occurred for AuNR-S-PEG_8-COOH, and immediate aggregation was observed for AuNR-citrate, suggesting loose and labile coatings.

Regarding ionic strength, AuNR-X_4C_4, AuNR-S-PEG_8-COOH and AuNR-CTAB were both stable after addition of at least 300 mM NaCl, while AuNR-citrate immediately and strongly aggregated under the same conditions (Fig. S7D and S8A†).

The impact of high temperature on AuNR colloids stability was also evaluated over the course of 15 h (Fig. 2C and S7C†). An arbitrary temperature of 90 °C was chosen to exert signifi-

 This journal is © The Royal Society of Chemistry 2024

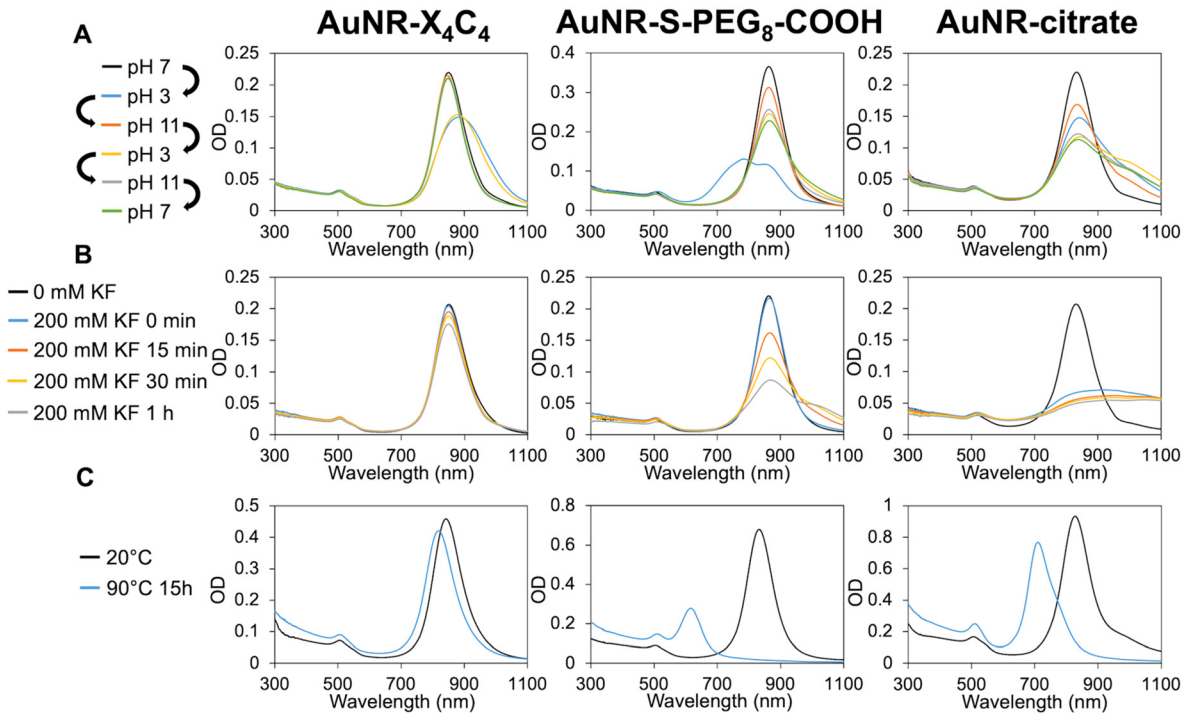

Fig. 2 Stability of AuNR-X_4C_4 (left), AuNR-S-PEG_8-COOH (middle) and AuNR-citrate (right) regarding (A) successive pH variations, (B) 200 mM KF incubation and (C) heating at 90 °C.

cant stress to AuNR colloids while staying below the boiling point of water. After 15 h at 90 °C, an important hypsochromic shift was observed for AuNR-S-PEG_8-COOH ($\Delta\lambda_{LSPR}$ = 217 nm) and AuNR-citrate ($\Delta\lambda_{LSPR}$ = 118 nm), while a much slighter one was observed for AuNR-X_4C_4 ($\Delta\lambda_{LSPR}$ = 23 nm) and AuNR-CTAB ($\Delta\lambda_{LSPR}$ = 25 nm). TEM analysis was performed before and after heating the suspensions to assess potential AuNR deformation (Fig. S9†). As expected, an important decrease in AR was observed for AuNR-S-PEG_8-COOH (3.4 ± 0.7 before and 2.4 ± 0.4 after heating) and AuNR-citrate (3.3 ± 0.9 before and 2.6 ± 0.6 after heating), while no AR change was observed for AuNR-X_4C_4 (3.6 ± 0.7 before and 3.6 ± 0.6 after heating) and AuNR-CTAB (3.6 ± 1.1 before and 3.6 ± 0.8 after heating). The observed shortening of the AuNRs is attributed to Ostwald ripening, and also likely due to the progressive thermolysis of the Au–S bond for AuNR-S-PEG_8-COOH.[44,45] These observations suggest that the calixarene and CTAB coating grant better resistance towards heat-mediated deformation than thiolated PEG coatings or adsorbed citrate molecules.

AuNR-X_4C_4, AuNR-S-PEG_8-COOH and AuNR-CTAB could both be dried in the presence of sucrose as a lyoprotecting agent and redispersed in water without significant aggregation or reduction of OD_{LSPR}, unlike AuNR-citrate (Fig. S7E and S8B†). Briefly, the AuNR suspensions were incubated with 10 wt% sucrose before drying them under reduced pressure. Once dried, the AuNRs were redispersed with water and sonicated before recording their UV-visible spectra.

Furthermore, ageing of AuNR-X_4C_4 was evaluated at room temperature for at least 12 months. No significant changes in their UV-visible absorption spectra could be noticed, while AuNR-S-PEG_8-COOH experienced a hypsochromic shift of their longitudinal LSPR band. A similar behaviour was observed for AuNR-citrate along with an important decrease in OD_{LSPR} and widening of the longitudinal LSPR band, indicating aggregation (Fig. S8C†). For AuNR-CTAB, only a slight reduction of OD_{LSPR} was observed (Fig. S7F†).

Overall, AuNR-X_4C_4 demonstrate remarkable stability compared to commonly used AuNRs. This property is attributed to the robust organic layer formed through the formation of multiple Au–C covalent bonds with the gold surface by the calixarene, but also to the higher stability of the Au–C bond compared to the more labile Au–S bond.[29,30,46]

Covalent conjugation of molecules to AuNR-X_4C_4

An additional advantage conferred by the X_4C_4 coating lies in the presence of appending carboxylate groups on the small rim of the calixarenes, enabling the coupling of amine-terminated molecules through a peptide-type coupling reaction. As proof of concept, an aminated fluorophore (Cyanine5.5 amine) was conjugated onto AuNR-X_4C_4 *via* a carbodiimide cross-linking reaction using EDC and sulfo-NHS. A control experiment was conducted under identical conditions, without addition of coupling reagents to the reaction mixture. Each reaction was performed in triplicates. The fluorophore absorbs light in a spectral region where the absorbance of the AuNRs is minimal (λ_{max} = 684 nm; ε = 198 000 L mol^{-1} cm^{-1}), allowing for its quantification (see the Supplementary Methods section of the ESI† for the detailed procedure). Despite multiple cen-

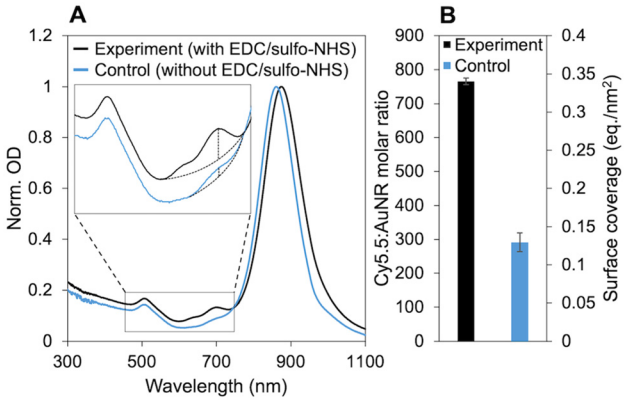

Fig. 3 Covalent conjugation of AuNR-X_4C_4 with Cyanine5.5 amine. (A) UV-visible absorption spectra without (blue line) and with coupling reagents (black line). (B) Quantification of conjugated Cyanine5.5 amine molecules with standard deviation error bars without (blue) and with coupling reagents (black).

trifugation and resuspension cycles using sodium dodecyl sulfate (SDS), a small amount of the fluorophore was observed on the AuNRs in the absence of coupling reagents. This residual amount could be attributed to the strong adsorption of the fluorophore on the organic coating or the gold surface. However, the UV-visible absorption bands of the fluorophore are much more pronounced and distinctly visible in the presence of coupling reagents compared to the control, indicating successful coupling (Fig. 3A). With the addition of coupling reagents, a loading of 770 ± 10 Cyanine5.5 per AuNR was calculated (0.34 ± 0.01 Cy5.5 per nm^2), whereas 290 ± 30 Cyanine5.5 per AuNR (0.13 ± 0.01 Cy5.5 per nm^2) was calculated for the control experiment (Fig. 3B). By subtracting these two values, an average covalent loading of 480 ± 30 Cyanine5.5 per AuNR (0.21 ± 0.01 Cy5.5 per nm^2) was obtained. The addition of coupling reagents resulted in an almost three-fold increase in loading, indicating that AuNR-X_4C_4 can be covalently conjugated with amine-terminated molecules while preserving their colloidal stability. Additionally, a slight bathochromic shift of the longitudinal LSPR band was observed in presence of coupling reagents, which is attributed to modification of the dielectric environment at the surface of AuNRs upon fluorophore conjugation.

AuNR-X_4C_4 as photothermal agents

The photothermal properties of AuNR-X_4C_4 were investigated in aqueous medium and compared to those of AuNRs stabilized with thiolated PEG molecules, citrate, or CTAB. The AuNRs colloidal suspensions (OD_{808} = 0.5; ~0.1 nM) were irradiated with an 808 nm continuous diode laser with a power density of 3 W cm^{-2} for 18 min. Then the laser was subsequently switched off for a cooling period of 18 min. The variation of temperatures during the cycles were monitored with a thermocouple (Fig. 4A and S11A†). To determine photothermal efficiency (η), thermal equilibrium must be reached, *i.e.* the maximum temperature T_{max} that can be reached at a constant value. The difference between T_{max} and the ambient temperature ($\Delta T_{max} = T_{max} - T_{amb}$) is used as a photothermal marker. Thermal equilibrium is reached in 18 min for all colloids. High maximum temperatures ranging from 62.3 °C to 90.4 °C have been measured upon laser irradiation for the different AuNRs suspensions. AuNR-X_4C_4, AuNR-S-PEG_8-COOH and AuNR-citrate reached relatively similar maximum temperatures of 88.5 °C (ΔT_{max} = 66.8 °C), 90.4 °C (ΔT_{max} = 70.8 °C), and 83.9 °C (ΔT_{max} = 61.6 °C), respectively, while AuNR-CTAB reached a substantially lower maximum temperature of 62.3 °C (ΔT_{max} = 39.9 °C). However, the temperature plateau was rapidly reached for AuNR-CTAB (~8 min), with the temperature starting to slowly decrease afterward, indicating a loss in photothermal performance. As expected, generated heat was increased with AuNR concentration and with laser power density (Fig. S10†). In the absence of AuNRs, ultrapure water exhibited a maximum temperature of only 22.1 °C (ΔT_{max} = 4.7 °C) under the same irradiation conditions (Fig. S12A†), indicating the strong photothermal activity of the AuNRs at 808 nm. No fatigue was observed after several successive heating and cooling cycles for AuNR-X_4C_4, AuNR-S-PEG_8-COOH, and AuNR-citrate while substantial fatigue was observed for AuNR-CTAB (Fig. S13†).

Photothermal conversion efficiencies (η) were calculated according to the following equation reported by Roper *et al.* (eqn (1)):[35]

$$\eta\,(\%) = 100 \times \frac{hS(T_{max} - T_{amb}) - Q_0}{I(1 - 10^{-A_\lambda})} \quad (1)$$

where h is the heat transfer coefficient, S the heat transfer surface area, T_{max} the maximum temperature, T_{amb} the ambient temperature, Q_0 the heat dissipated by the solvent, I the incident laser power and A_λ the absorbance of the photothermal absorber at the irradiation wavelength. The system time constant for heat transfer τ_s is equal to $\left(\sum_i m_i C_{p,i}\right)/(hS)$, where $m_i C_{p,i}$ are the products of mass and heat capacity of the system components i (water and glass cuvette, the contribution of the gold was found to be negligible). τ_s was determined by plotting the cooling period (from 1080 to 2160 s) as a function of $-\ln(\Delta T/\Delta T_{max})$ (Fig. S11B and S12B†) where ΔT is the difference between the measured temperature T and ambient temperature T_{amb}. It was then used to obtain the hS coefficient for calculating η. An example of photothermal conversion efficiency calculation is detailed in the Supplementary Methods section of the ESI.†

The calculated photothermal conversion efficiencies are 89% ± 3% for AuNR-X_4C_4, 88% ± 4% for AuNR-S-PEG_8-COOH, 87% ± 3% for AuNR-citrate and 54% ± 3% for AuNR-CTAB. Except for AuNR-CTAB having a much lower photothermal efficiency, the other AuNRs exhibited similar η values regardless of their coating. It is worth noting that the absolute values of calculated photothermal conversion efficiencies are heavily dependent on the experimental setup and the calculation method,[47] and can therefore only be objectively compared

 This journal is © The Royal Society of Chemistry 2024

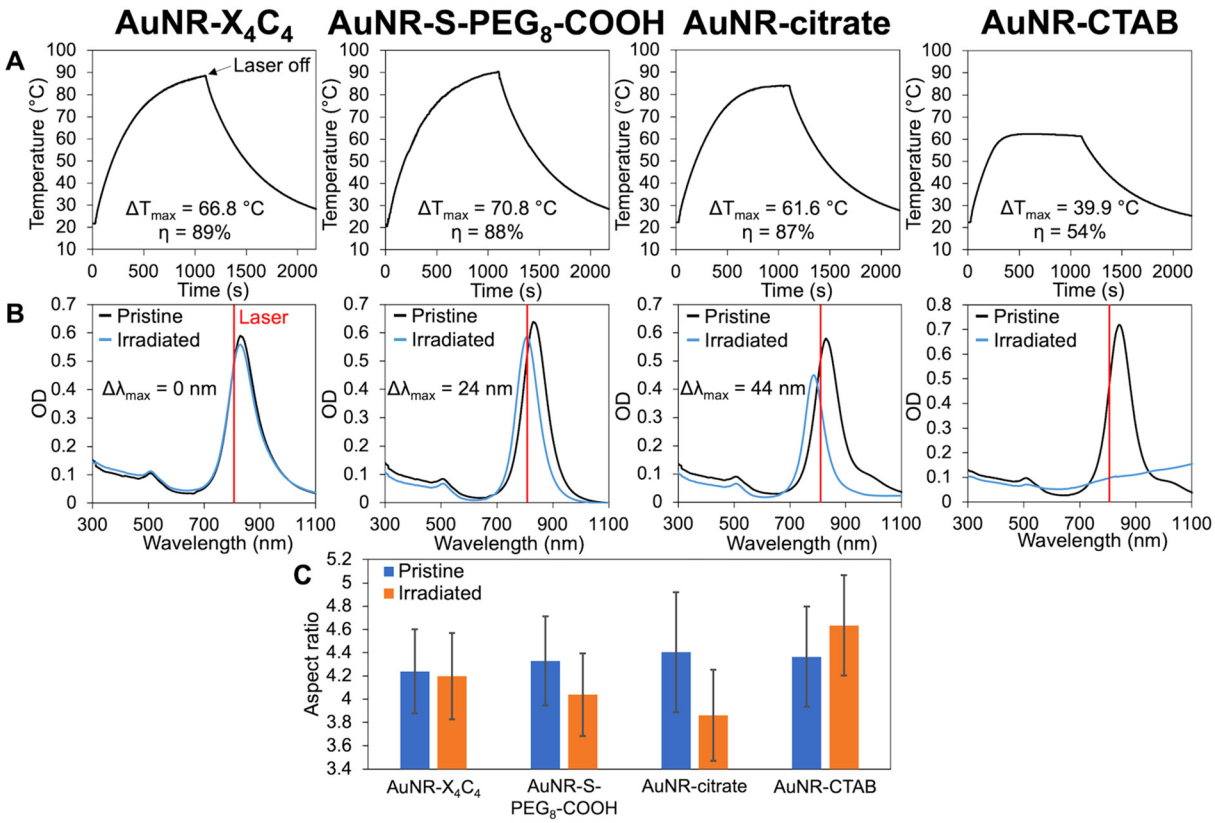

Fig. 4 Photothermal stability of different AuNRs. (A) Temperature profiles recorded on aqueous solutions of AuNRs (OD_{808} = 0.5) when illuminated with a continuous 808 nm diode laser (3 W cm^{-2}) for 18 min and after turning the laser off for 18 min. (B) UV-visible absorption spectra of AuNRs before (black line) and after (blue line) irradiation. (C) AuNR aspect ratio variations measured by TEM before (blue) and after (orange) irradiation with standard deviation error bars. The reported aspect ratio values represent the averages calculated from more than 100 individual AuNR aspect ratio values measured from TEM images, except for AuNR-CTAB after irradiation because the sample was too aggregated to analyse more than a few individual rods.

when obtained from the same setup and method. This could explain the important discrepancies of the reported photothermal conversion efficiency values in the literature, which can range from 20% to over 90% for AuNRs.[48–51]

Interestingly, we have compared the UV-visible absorption spectra of the AuNR colloidal suspensions before and after irradiation. The spectra display striking differences (Fig. 4B). For AuNR-X_4C_4, only a slight reduction of OD_{LSPR} is observed but the maximum absorption wavelength of the longitudinal LSPR band remains constant ($\Delta\lambda_{LSPR}$ = 0 nm). For AuNR-S-PEG_8-COOH and AuNR-citrate, a larger reduction of OD_{LSPR} is observed and, more importantly, a substantial hypsochromic shift ($\Delta\lambda_{LSPR}$ = 24 nm and $\Delta\lambda_{LSPR}$ = 44 nm, respectively) occurs. This observation can be explained by AuNR deformation leading to a decrease in AR (decrease in length and increase in width) during irradiation.[44,45] For AuNR-CTAB, no defined longitudinal LSPR band was observed after irradiation, suggesting AuNR aggregation, correlating with the poor photothermal performance compared to the other tested AuNRs. The slightly higher maximum temperature for AuNR-S-PEG_8-COOH compared to AuNR-X_4C_4 can therefore be attributed to the increase of OD_{808} during irradiation, as observed in the UV-visible absorption spectrum, which is linked to their deformation. To confirm these findings, TEM images of AuNRs were recorded before and after irradiation (Fig. S14†). No significant change in AR was observed for AuNR-X_4C_4 (4.3 ± 0.4 before and 4.2 ± 0.4 after irradiation) (Fig. 4C). A more substantial decrease in AR was observed for AuNR-S-PEG_8-COOH (4.3 ± 0.4 before and 4.0 ± 0.4 after irradiation) and for AuNR-citrate (4.4 ± 0.5 before and 3.9 ± 0.4 after irradiation). For AuNR-CTAB, individual AuNRs could still be observed after irradiation, but they were more agglomerated than before irradiation, consistent with the changes observed in their UV-visible absorption spectrum. Surprisingly, an increase in AR was observed (4.4 ± 0.4 before and 4.6 ± 0.4 after irradiation), although their sizes were more difficult to estimate from TEM images due to AuNR agglomeration. In addition, these observations were corroborated by dynamic light scattering (DLS) measurements (Fig. S15†), which indicate a pronounced increase in the hydrodynamic radius after irradiation for AuNR-CTAB. In contrast, AuNR-X_4C_4 exhibits remarkable stability in both its rotational and translational diffusion radii, unlike AuNR-S-PEG_8-COOH and AuNR-citrate, which show a slight decrease in these values. The DLS behaviour is consist-

ent with the TEM observations. The low photothermal conversion efficiency of AuNR-CTAB compared to other AuNRs, as well as their substantial fatigue over several successive heating and cooling cycles, can be explained by their aggregation upon irradiation, as evidenced by the UV-visible spectra (Fig. 4B, right panel), TEM images (Fig. S14,† right panels), and DLS data (Fig. S15,† bottom right panel). As shown in the UV-visible spectra before and after irradiation, the OD_{808} of AuNR-CTAB decreases significantly upon irradiation, thereby reducing their photothermal activity because the AuNRs do not absorb as much incident light. This inevitably leads to a lower photothermal conversion efficiency. In contrast, no significant aggregation was observed for the other AuNRs, which explains their high photothermal conversion efficiency compared to AuNR-CTAB and their consistent heating over several irradiation cycles, as they maintain much higher OD_{808} upon irradiation.

The surface chemistry of the AuNRs was further investigated through X-ray photoelectron spectroscopy (XPS) measurements to evidence any impact of the laser irradiation on the coating. Herein, we only report the results obtained for AuNR-X_4C_4 and AuNR-S-PEG_8-COOH since photothermal measurements for the two other series of AuNRs (AuNR-citrate and AuNR-CTAB) have been performed in suspensions containing citrate and CTAB, respectively, where the free ligands may interfere in the XPS analyses. Fig. 5 shows the high-resolution core level spectra in the C 1s region for AuNR-X_4C_4 and AuNR-S-PEG_8-COOH and in the S 2p region for the latter. Peak-fitting of the C 1s photoelectron signal was performed to reveal the molecular fingerprint of the coating before and after irradiation. Worth is noting that the XPS analyses for the 4 series of AuNRs before laser irradiation demonstrate the successful exchange of CTAB to the various coatings (Fig. 5A, C and S17, S18†). More specifically, the C 1s signals of a deposit of AuNR-X_4C_4 and AuNR-S-PEG_8-COOH could be decomposed in CC-CH (284.4–285.5 eV), COC/CS (286.3–286.5 eV), C═O (287.6–288.1 eV) and OC═O (289.1–289.3 eV) components. Before irradiation, the ratio of OC═O/COC components are in fair agreement with the theoretical values considering the chemical structure of X_4C_4 (0.5) and S-PEG_8-COOH (0.059, including the C–S contribution), respectively (Fig. 5A and C). We experimentally found OC═O/COC equal to 0.4 for AuNR-X_4C_4 and 0.08 for AuNR-S-PEG_8-COOH. Carbonaceous contamination species are also always observed in XPS spectra explaining the presence of CC–CH, C═O, COC or OC═O components in higher concentrations than expected from the chemical structures of the coating molecules. The photoelectron signal S 2p was also recorded in the case of AuNR-S-PEG_8-COOH (Fig. 5E and F). The signal of weak intensity is observed in the range 161.9–163.9 eV with a main doublet contribution at 161.9 and 163.0 eV, characteristic of gold-bound thiolate species while a smallest contribution at higher binder energy (163.8–164 eV) is probably due to flat-lying physisorbed HS-PEG_8-COOH molecules (unbound sulfur species).[52,53] Only a very weak contribution could be seen at 168–169 eV due to oxidized sulfur termini. After laser irradiation, no significant

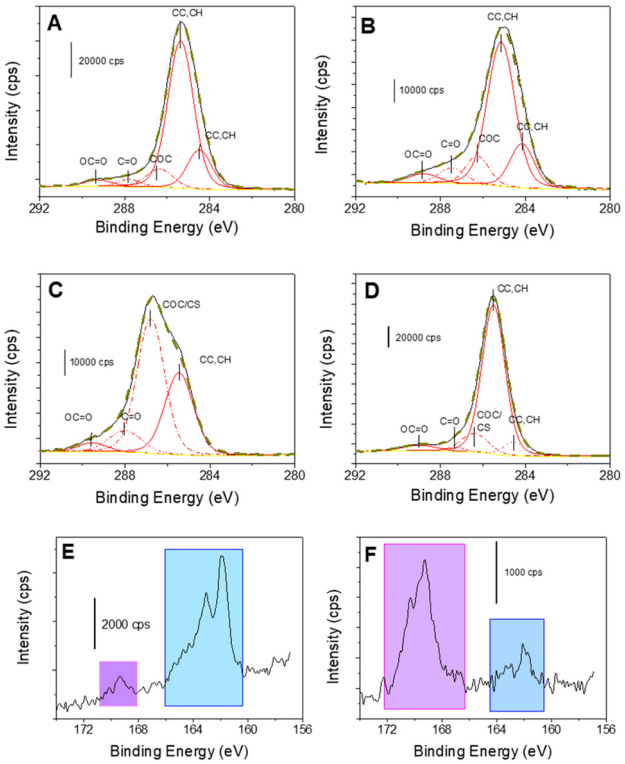

Fig. 5 High-resolution peak-fitted C 1s core level spectra of deposits of AuNR-X_4C_4 (A and B) and AuNR-S-PEG_8-COOH (C and D) colloids before (A and C) and after (B and D) continuous 808 nm laser irradiation at 3 W cm^{-2}. High-resolution core level S 2p spectra for AuNR-S-PEG_8-COOH before (E) and after irradiation (F). Violet and blue highlights correspond to oxidized sulfur and thiolate-gold molecules, respectively.

change is evidenced in the C 1s spectrum corresponding to AuNR-X_4C_4 (Fig. 5A *vs.* Fig. 5B), showing the strong stability of the coating. In sharp contrast, the C 1s spectrum of the deposit of AuNR-S-PEG_8-COOH is strongly modified after irradiation (Fig. 5C *vs.* Fig. 5D). Moreover, the signal in the S 2p region now shows a main component centred at 168.4 eV attributable to oxidized sulfur, along with a drastic decrease of the gold-bound thiolate contribution (Fig. 5F). These XPS data indicate that the S-PEG_8-COOH coating is heavily affected by the laser irradiation.

Overall, these findings indicate that calixarene-stabilized AuNRs can withstand continuous laser irradiation over extended periods without undergoing deformation or degradation of the metallic structure and its coating unlike conventional AuNRs. This superior stability positions calixarene-coated AuNRs as promising candidates for applications in photothermal therapy.

Conclusions

In summary, gold nanorods were successfully synthesized through seed-mediated growth. The symmetry-breaking event is decoupled from the seeded growth process, enabling lower

This journal is © The Royal Society of Chemistry 2024

polydispersity and improved shape yield compared to standard methodologies. Efficient and reproducible CTAB ligand exchange with calix[4]arene-tetradiazonium $X_4C_4(N_2^+)_4$ was achieved by reductive grafting, involving careful optimization of reaction conditions, including pH, free CTAB concentration, and AuNR concentration. The confirmation of calixarene grafting and CTAB removal was ascertained by ATR-FTIR, SERS and XPS spectroscopies and ζ-potential measurements, while the retention of colloidal stability was verified by UV-visible spectroscopy and TEM observations. Furthermore, the calixarene layer enabled the covalent conjugation of amine-terminated molecules onto the AuNRs, enabling opportunities for specific targeting and drug delivery. These calixarene-coated AuNRs demonstrated excellent chemical and colloidal stability against various physicochemical stresses, outperforming commonly used AuNRs. This stability is attributed to the formation of multiple Au–C bonds between the calixarenes and the gold surface, and their irreversible nature.[22–24,26] Notably, these novel AuNRs exhibited resistance to deformation under continuous laser irradiation, maintaining their optical properties and dimensions throughout prolonged illumination. The calixarene coating is not impacted by laser irradiation in sharp contrast to thiolate coating. In addition to the thermolysis of the Au–S bond as demonstrated by XPS analyses and known thermal desorption of labile ligands like citrate,[16,54] the deformation of AuNRs under laser irradiation could lead to the additional leaching of adsorbed molecules and gold etching, potentially resulting in undesirable effects in biological systems. The use of calixarene-coated AuNRs presents a potential solution to alleviate these issues, offering enhanced reliability and control in photothermal therapy or photoinduced drug delivery. Calixarenes have already been used for biomedical applications with little to no toxicity observed,[55] so there is no reason to believe that AuNR-X_4C_4 would induce significant toxicity. Nonetheless, their biocompatibility and cytotoxicity would need to be assessed before transitioning into biological systems. Beyond the scope of this work, owing to their remarkable stability, chemical functionality suitable for conjugation chemistry, and robustly anchored thin coating, these calixarene-coated AuNRs could prove promising for numerous other applications such as targeted bioimaging, photodynamic therapy, stimuli-responsive drug delivery (*e.g.* light or pH-triggered), (bio)sensing, photoelectrocatalysis, or optoelectronics. Notably, the reversible pH-mediated aggregation behaviour of AuNR-X_4C_4 could be leveraged for the development of tumour microenvironment specific PTAs, contrast agents for imaging and drug carriers.[56–58]

Author contributions

V. L. synthesized the gold nanorod samples, conducted and analysed the characterizations and stability tests. M. R. recorded additional TEM images. F. C. and V. L. designed and analysed the photothermal experiments, which were conducted by V. L. C. L. performed and analysed the XPS measurements. V. L., G. B. and I. J. designed the manuscript, which was then edited by all co-authors. G. B. and I. J. have conceptualized and supervised the work.

Data availability

The data underlying this study are available in the published article and its ESI.†

Conflicts of interest

There are no conflicts to declare.

Acknowledgements

This research was supported by the Fonds pour la formation à la Recherche dans l'Industrie et dans l'Agriculture (FRIA-FRS) (PhD grant to V. L.). The TEM and XPS measurements have been performed on THEMIS and ASPHERYX platforms, respectively (ScanMAT, UAR 2025 Univ. Rennes-CNRS, CPER-FDER 2015–2020 and CPER MAT & Trans 2021–2027) and were funded by the Agence Nationale pour la Recherche (MARCEL project, grant number ANR-21-CE50-0034-MARCEL). The photothermal studies were done on the Δlight (deltalight) platform dedicated to photothermal studies in Rennes (ISCR, UMR 6226). L. Rault (ScanMAT, UAR 2025 and ISCR, UMR 6226, Rennes) is gratefully acknowledged for recording the TEM images, SAED patterns and EDX spectra.

References

1 A. T. Haine and T. Niidome, *Chem. Pharm. Bull.*, 2017, **65**, 625–628.
2 V. S. Marangoni, J. Cancino-Bernardi and V. Zucolotto, *J. Biomed. Nanotechnol.*, 2016, **12**, 1136–1158.
3 J. Zheng, X. Cheng, H. Zhang, X. Bai, R. Ai, L. Shao and J. Wang, *Chem. Rev.*, 2021, **121**, 13342–13453.
4 N. U. Khan, J. Lin, M. R. Younas, X. Liu and L. Shen, *Cancer Nanotechnol.*, 2021, **12**, 20.
5 H. Chen, L. Shao, Q. Li and J. Wang, *Chem. Soc. Rev.*, 2013, **42**, 2679–2724.
6 S. Liao, W. Yue, S. Cai, Q. Tang, W. Lu, L. Huang, T. Qi and J. Liao, *Front. Pharmacol.*, 2021, **12**, 664123.
7 R. Zhou, M. Zhang, J. Xi, J. Li, R. Ma, L. Ren, Z. Bai, K. Qi and X. Li, *Nanoscale Res. Lett.*, 2022, **17**, 68.
8 D. Harris-Birtill, M. Singh, Y. Zhou, A. Shah, P. Ruenraroengsak, M. E. Gallina, G. B. Hanna, A. E. G. Cass, A. E. Porter, J. Bamber and D. S. Elson, *PLoS One*, 2017, **12**, e0185990.
9 Y. Horiguchi, K. Honda, Y. Kato, N. Nakashima and Y. Niidome, *Langmuir*, 2008, **24**, 12026–12031.
10 A. S. D. S. Indrasekara, R. C. Wadams and L. Fabris, *Part. Part. Syst. Charact.*, 2014, **31**, 819–838.

11 D. Fernando, S. Sulthana and Y. Vasquez, *ACS Appl. Bio Mater.*, 2020, **3**, 1374–1384.
12 L. Wang, X. Jiang, Y. Ji, R. Bai, Y. Zhao, X. Wu and C. Chen, *Nanoscale*, 2013, **5**, 8384–8391.
13 S. Chen, M. Yang, S. Hong and C. Lu, *Nanoscale*, 2014, **6**, 3197–3205.
14 J. G. Mehtala, D. Y. Zemlyanov, J. P. Max, N. Kadasala, S. Zhao and A. Wei, *Langmuir*, 2014, **30**, 13727–13730.
15 K. Liu, Y. Zheng, X. Lu, T. Thai, N. A. Lee, U. Bach and J. J. Gooding, *Langmuir*, 2015, **31**, 4973–4980.
16 F. Li, H. Zhang, B. Dever, X.-F. Li and X. C. Le, *Bioconjugate Chem.*, 2013, **24**, 1790–1797.
17 N. Bhatt, P.-J. J. Huang, N. Dave and J. Liu, *Langmuir*, 2011, **27**, 6132–6137.
18 A. Chompoosor, G. Han and V. M. Rotello, *Bioconjugate Chem.*, 2008, **19**, 1342–1345.
19 X. Shi, H. L. Perry and J. D. E. T. Wilton-Ely, *Nanotheranostics*, 2021, **5**, 155–165.
20 H.-C. Huang, S. Barua, D. B. Kay and K. Rege, *ACS Nano*, 2009, **3**, 2941–2952.
21 M. Tebbe, C. Kuttner, M. Männel, A. Fery and M. Chanana, *ACS Appl. Mater. Interfaces*, 2015, **7**, 5984–5991.
22 A. Mattiuzzi, I. Jabin, C. Mangeney, C. Roux, O. Reinaud, L. Santos, J.-F. Bergamini, P. Hapiot and C. Lagrost, *Nat. Commun.*, 2012, **3**, 1130.
23 L. Troian-Gautier, A. Mattiuzzi, O. Reinaud, C. Lagrost and I. Jabin, *Org. Biomol. Chem.*, 2020, **18**, 3624–3637.
24 L. Troian-Gautier, A. Mattiuzzi, P. Blond, M. Retout, G. Bruylants, O. Reinaud, C. Lagrost and I. Jabin, in *Aryl Diazonium Salts and Related Compounds: Surface Chemistry and Applications*, ed. M. M. Chehimi, J. Pinson and F. Mousli, Springer International Publishing, Cham, 2022, pp. 247–262.
25 *Calixarenes 2001*, ed. Z. Asfari, V. Böhmer, J. Harrowfield, J. Vicens and M. Saadioui, Springer Netherlands, Dordrecht, 2001.
26 L. Troian-Gautier, H. Valkenier, A. Mattiuzzi, I. Jabin, N. V. Den Brande, B. V. Mele, J. Hubert, F. Reniers, G. Bruylants, C. Lagrost and Y. Leroux, *Chem. Commun.*, 2016, **52**, 10493–10496.
27 B. Gosselin, M. Retout, R. Dutour, L. Troian-Gautier, R. Bevernaegie, S. Herens, P. Lefèvre, O. Denis, G. Bruylants and I. Jabin, *Anal. Chem.*, 2022, **94**, 7383–7390.
28 M. Retout, B. Gosselin, A. Adrović, P. Blond, I. Jabin and G. Bruylants, *Nanoscale*, 2023, **15**, 11981–11989.
29 E. De La Llave, A. Ricci, E. J. Calvo and D. A. Scherlis, *J. Phys. Chem. C*, 2008, **112**, 17611–17617.
30 S. A. Orefuwa, M. Ravanbakhsh, S. N. Neal, J. B. King and A. A. Mohamed, *Organometallics*, 2014, **33**, 439–442.
31 M. Nguyen, I. Kherbouche, S. Gam-Derouich, I. Ragheb, S. Lau-Truong, A. Lamouri, G. Lévi, J. Aubard, P. Decorse, N. Félidj and C. Mangeney, *Chem. Commun.*, 2017, **53**, 11364–11367.
32 R. Ahmad, L. Boubekeur-Lecaque, M. Nguyen, S. Lau-Truong, A. Lamouri, P. Decorse, A. Galtayries, J. Pinson, N. Felidj and C. Mangeney, *J. Phys. Chem. C*, 2014, **118**, 19098–19105.
33 J. Pinson and F. Podvorica, *Chem. Soc. Rev.*, 2005, **34**, 429–439.
34 B. Gosselin, G. Bruylants and I. Jabin, *ACS Appl. Nano Mater.*, 2024, **7**, 6169–6177.
35 D. K. Roper, W. Ahn and M. Hoepfner, *J. Phys. Chem. C*, 2007, **111**, 3636–3641.
36 G. González-Rubio, V. Kumar, P. Llombart, P. Díaz-Núñez, E. Bladt, T. Altantzis, S. Bals, O. Peña-Rodríguez, E. G. Noya, L. G. Macdowell, A. Guerrero-Martínez and L. M. Liz-Marzán, *ACS Nano*, 2019, **13**, 4424–4435.
37 M. Retout, P. Blond, I. Jabin and G. Bruylants, *Bioconjugate Chem.*, 2021, **32**, 290–300.
38 H. Valkenier, V. Malytskyi, P. Blond, M. Retout, A. Mattiuzzi, J. Goole, V. Raussens, I. Jabin and G. Bruylants, *Langmuir*, 2017, **33**, 8253–8259.
39 J. He, S. Unser, I. Bruzas, R. J. Cary, Z. Shi, R. Mehra, K. Aron and L. Sagle, *Colloids Surf., B*, 2018, **163**, 140–145.
40 A. Tetenoire, A. Omelchuk, V. Malytskyi, I. Jabin, V. Lepeintre, G. Bruylants, Y. Luo, A. Fihey, M. Kepenekian and C. Lagrost, *Chem. Sci.*, 2024, DOI: **10.1039/D4SC02355B**.
41 G. Socrates, *Infrared and Raman Characteristic Group Frequencies: Tables and Charts*, Wiley, Chichester, England, 3rd edn, 2001.
42 S. Lee, L. J. E. Anderson, C. M. Payne and J. H. Hafner, *Langmuir*, 2011, **27**, 14748–14756.
43 M. Retout, B. Gosselin, J. V. Jokerst, I. Jabin and G. Bruylants, *Colloids Surf., A*, 2023, **660**, 130801.
44 R. Zou, Q. Zhang, Q. Zhao, F. Peng, H. Wang, H. Yu and J. Yang, *Colloids Surf., A*, 2010, **372**, 177–181.
45 J. Huang, P. Mao, P. Ma, Y. Pu, C. Chen and Z. Xia, *Optik*, 2016, **127**, 10343–10347.
46 L. Laurentius, S. R. Stoyanov, S. Gusarov, A. Kovalenko, R. Du, G. P. Lopinski and M. T. McDermott, *ACS Nano*, 2011, **5**, 4219–4227.
47 A. Paściak, A. Pilch-Wróbel, Ł. Marciniak, P. J. Schuck and A. Bednarkiewicz, *ACS Appl. Mater. Interfaces*, 2021, **13**, 44556–44567.
48 A. Paściak, R. Marin, L. Abiven, A. Pilch-Wróbel, M. Misiak, W. Xu, K. Prorok, O. Bezkrovnyi, Ł. Marciniak, C. Chanéac, F. Gazeau, R. Bazzi, S. Roux, B. Viana, V.-P. Lehto, D. Jaque and A. Bednarkiewicz, *ACS Appl. Mater. Interfaces*, 2022, **14**, 33555–33566.
49 X. Wang, G. Li, Y. Ding and S. Sun, *RSC Adv.*, 2014, **4**, 30375–30383.
50 M. Almada, B. H. Leal-Martínez, N. Hassan, M. J. Kogan, M. G. Burboa, A. Topete, M. A. Valdez and J. Juárez, *Mater. Sci. Eng., C*, 2017, **77**, 583–593.
51 X. Liu, B. Li, F. Fu, K. Xu, R. Zou, Q. Wang, B. Zhang, Z. Chen and J. Hu, *Dalton Trans.*, 2014, **43**, 11709.
52 D. G. Castner, K. Hinds and D. W. Grainger, *Langmuir*, 1996, **12**, 5083–5086.
53 T. Ishida, M. Hara, I. Kojima, S. Tsuneda, N. Nishida, H. Sasabe and W. Knoll, *Langmuir*, 1998, **14**, 2092–2096.

 This journal is © The Royal Society of Chemistry 2024

54 J.-W. Park and J. S. Shumaker-Parry, *ACS Nano*, 2015, **9**, 1665–1682.
55 Y. Pan, X. Hu and D. Guo, *Angew. Chem., Int. Ed.*, 2021, **60**, 2768–2794.
56 S. Park, W. J. Lee, S. Park, D. Choi, S. Kim and N. Park, *Sci. Rep.*, 2019, **9**, 20180.
57 S. Li, K.-H. Lui, T.-H. Tsoi, W.-S. Lo, X. Li, X. Hu, W. Chi-Shing Tai, C. Hiu-Ling Hung, Y.-J. Gu and W.-T. Wong, *Nanoscale Adv.*, 2019, **1**, 554–564.
58 J. Wang, H. Wang, L. Yan, Z. Hu, X. Wu and F. Li, *RSC Adv.*, 2019, **9**, 5270–5281.

This journal is © The Royal Society of Chemistry 2024